Dynamics of gaseous oxidized mercury at Villum Research Station during the High Arctic summer

Jakob Boyd Pernov, Bjarne Jensen, Andreas Massling, Daniel Charles Thomas, and Henrik Skov

Department of Environmental Science, iClimate, Arctic Research Center, Aarhus University, Frederiksborgvej 399, 4000
5 Roskilde, Denmark

Correspondence: Jakob Boyd Pernov (jbp@envs.au.dk)

Abstract. While much research has been devoted to the subject of gaseous elemental mercury (GEM) and gaseous oxidized mercury (GOM) in the Arctic spring, during atmospheric mercury depletion events, few studies have examined the behavior of GOM in the High Arctic summer. GOM, once introduced into the ecosystem, can pose a threat to human and wildlife health,
10 though there remain large uncertainties regarding the transformation, deposition, and assimilation of mercury into the ecosystem. Therefore, to further our understanding of the dynamics of gaseous oxidized mercury in the High Arctic during the late summer, we performed measurements of GEM and GOM along with meteorological parameters, atmospheric constituents, and air mass history during two summer campaigns in 2019 and 2020 at Villum Research Station (Villum) in Northeastern Greenland. Five events of enhanced GOM concentrations were identified and investigated in greater detail. The origin of these
15 events was identified, through analysis of air mass back-trajectories, associated meteorological data, and other atmospheric constituents, to be the cold, dry free troposphere. These events were associated with low RH, limited precipitation, cold temperatures, and intense sunlight along the trajectory path. Events were positively correlated with ozone, aerosol particle number, and black carbon mass concentration, which were interpreted as an indication of tropospheric air masses. This work aims to provide a better understanding of the dynamics of GOM during the High Arctic summer.

1 Introduction

20 Gaseous elemental mercury (Hg^0 or GEM) is a ubiquitous pollutant in the atmosphere due to its long relaxation time (6 to 12 months), thus being subject to long-range transport from source regions to remote environments through deposition and reemission cycling (Pirrone et al., 2010; Skov et al., 2020). The sources of mercury include anthropogenic emissions, e.g., fossil fuel combustion and small artisan gold mines, in addition to natural emissions such as volcanoes, biomass burning, ocean
25 and soil evasion, and reemission of previously deposited mercury (AMAP, 2011). In the atmosphere, GEM is oxidized to its divalent form (Hg^{II}), commonly known as gaseous oxidized mercury (GOM). GOM has a much shorter residence time than GEM in the atmosphere owing to its higher solubility, lower vapor pressure, and faster deposition velocity (Skov et al., 2006). Mercury can also be present in aerosol particles, referred to as particulate bound mercury (PHg), either through GOM condensation or through heterogeneous reactions of GEM on aerosol surfaces (Durnford and Dastoor, 2011). In the polar

Atmospheric
Chemistry
and Physics
Discussions

30   regions, GEM typically dominates the atmospheric distribution throughout the year, with smaller contributions from GOM and PHg. However, during depletion events in the spring, GOM and PHg can constitute large fractions of total gaseous mercury. In contrast, in the mid-latitudes and especially in locations close to anthropogenic emission point sources, GOM and PHg can represent larger fractions of the atmospheric mercury burden (Muntean et al., 2018).

    In locations with elevated halogen concentrations (e.g., polar environments, coastal regions, volcanic plumes, and
35   salt lakes), GEM is quickly transformed into GOM (Angot et al., 2016). In the Arctic, this process manifests as atmospheric mercury depletion events (AMDEs), which occur in spring following polar sunrise, and result in the rapid depletion (on the order of hours) of GEM and conversion to GOM (Schroeder et al., 1998; Lindberg et al., 2002; Berg et al., 2003; Skov et al., 2004). In the early spring, this GOM is converted to PHg (through condensational processes due to the cold temperatures and high aerosol surface area) while in the late spring oxidized mercury is mainly present as GOM (due to reduced surface area
40   and increased temperatures) (Steffen et al., 2014). Late spring is also the peak of Hg in snow, indicating that GOM is the main deposition pathway (Lu et al., 2001; Steffen et al., 2014). GEM oxidization has been demonstrated to be initiated via photochemical reactions with the Br radical (R1-R2) through modeling studies (Holmes et al., 2006, 2010), kinetic studies (Donohoue et al., 2006), theoretical studies (Goodsite et al., 2004, 2012), and observations (Skov et al., 2004; Stephens et al., 2012; Wang et al., 2019).

45

$$Br + Hg^0 \leftrightarrow HgBr \qquad\qquad (R1)$$

$$HgBr + Y \rightarrow HgBrY \qquad\qquad (R2)$$

Where Y could be OH, O_3, NO_2, NO, HO_2, Br, Cl, BrO, ClO, I, IO, of which Br, I, and OH have been postulated to be the
50   main species for Y, both globally and in the Arctic (Goodsite et al., 2004, 2012). Sources of these reactive halogen species include emissions from sea ice, snowpack, frost flowers, refreezing leads, sea-salt aerosol, and liable halogen reservoir species (i.e., halocarbons and inorganic bromine) (Brooks et al., 2006; Kaleschke et al., 2004; Peterson et al., 2018, 2019; Simpson et al., 2015). The exact chemical formulas for GOM and PHg are currently unknown so both species are operationally defined by their detection methods (Landis et al., 2002; Angot et al., 2016). Once formed, GOM can either bind to aerosol particles,
55   becoming PHg, or deposit onto the snowpack through dry and wet deposition. Recently, isotope analysis has revealed GEM uptake by vegetation and soils to be the main source of mercury input to the terrestrial environment in Alaska (Obrist et al., 2010; Douglas and Blum, 2019; Jiskra et al., 2019), although this process has yet to be confirmed in the High Arctic. The majority of this deposited mercury is photo-reduced and emitted back into the atmosphere (Brooks et al., 2006; Dastoor et al., 2008; Kamp et al., 2018). The snowpack will retain a fraction of this mercury and release it with the ionic pulse during the
60   melt season, introducing mercury into the ecosystem (Ariya et al., 2004; Durnford and Dastoor, 2011).

    After deposition onto the Earth's surface, GEM, GOM, and PHg can be methylated through biotic and abiotic processes to organic mercury (methyl- and dimethylmercury) (Macdonald and Loseto, 2010; Møller et al., 2011). Organic mercury is an extremely powerful neurotoxin that bio-accumulates in upper trophic levels thus posing harmful effects to

Atmospheric
Chemistry
and Physics
Discussions

65 ecosystems and human health (especially in indigenous peoples in high latitudes and societies that rely heavily on a seafood diet) (Park and Zheng, 2012). Therefore, it is pertinent to understand mercury oxidation in response to a changing climate, especially in high latitude regions (Durnford and Dastoor, 2011; Stern et al., 2012).

While the majority of GOM formation and deposition occurs in the Arctic during spring, little attention has been given to the behavior of GOM outside of AMDEs. Steen et al. (2011) reported high amounts of GOM (max > 120 pg m^{-3}, mean 8 ± 13 pg m^{-3}) during the summers of 2007 and 2008 at Zeppelin Mountain (79.93° N 11.50° E, 474 m above sea level).

70 This study revealed a pattern of GOM previously unknown to the Arctic, with elevated GOM concentrations during the summer, which postulates GOM deposition occurs also outside of AMDEs. They concluded the presence of GOM was of local/regional origin, as transport of direct emissions from anthropogenic sources were unlikely. During a research expedition in the Arctic Ocean in June–August 2004, Aspmo et al. (2006) measured GEM, GOM, and PHg, and found increases in GEM over areas with > 70 % sea ice concentrations, which were attributed to an enhanced reduction potential and increased evasion

75 of supersaturated dissolved mercury from the ocean through open leads. They also found low levels of GOM (< 20 pg m^{-3}) and PHg (< 10 pg m^{-3}). Levels of Hg in snow and melt ponds were low (< 10 ng L^{-1}) suggesting little accumulation throughout the summer of deposited mercury from AMDEs in the spring. Concentrations of GEM, GOM, PHg, CO, and ozone were also reported on a research cruise throughout the Arctic basin from July–September 2005 (Sommar et al., 2010). They found low levels of GOM (3.2 ± 1.7 pg m^{-3}) and PHg (1.0 ± 0.7 pg m^{-3}), which were not correlated with GEM, sunlight, nor ozone.

80 Steffen et al. (2014) analyzed GOM and PHg at Alert, CA from 2002–2011, they reported low median values during July–September of 5.3–7.36 pg m^{-3} and 1.01–14.78 pg m^{-3} for PHg and GOM, respectively. The source of GOM during this study was unclear. These studies show that mercury oxidation and deposition can occur outside of the springtime AMDEs, therefore warranting further study.

The variability of GOM reported during the Arctic summer (Aspmo et al., 2006; Sommar et al., 2010) as well as the

85 previously unknown yearly cycle and lack of formation mechanism (Steen et al., 2011; Steffen et al., 2014) emphasize the need for further examination of the dynamics of GOM in the High Arctic summer. Resolving the sources and dynamics of mercury species in the High Arctic summer will help to infer the response of mercury in the context of a changing climate. It is also important to understand the dynamics of mercury to assess the effects of abatement strategies on atmospheric concentrations in the framework of the Minamata Convention (UNEP, 2013). This will aid in understanding what will be the

90 effects of decreasing anthropogenic mercury emissions and global climate change on the recycling of mercury between different environmental matrixes and how it is ultimately sequestered.

Here we report measurements of GEM and GOM, outside of AMDEs, during the late summer of 2019 and GEM and GOM as well as PHg in the late summer of 2020 at Villum Research Station (Villum). We investigate the levels of GOM in connection with meteorological parameters, ozone, aerosol particle physical properties, and air mass history and examine

95 existing interconnections and dependencies. In the following section, we describe the measurement site, analytical instrumentation, and analysis methods. We will then examine the behavior of GOM in relation to meteorological parameters and atmospheric constituents as well as air mass history. We compare our measurements to previous studies of GOM from the

mid-latitudes and hypothesize on possible halogen sources. We conclude with a summary and consider the implications for mercury oxidation in a future climate.

2 Methods and instrumentation

2.1 Measurement sites

Measurements were performed at Flyger's hut (N 81° 36′, W 16° 40′), which is part of Villum (81.6° N 16.67° W, 24 m above sea level) located on the Danish military base Station Nord in Northeastern Greenland. Villum and Flyger's hut are both located approx. 2 kilometers to the south of Station Nord, they are separated by approx. 200 meters distance and they are both upwind > 95% of the time from local pollution sources at the military base. All times are reported as UTC.

2.2 Atmospheric mercury measurements

In 2019, atmospheric measurements of GEM and GOM at Flyger's hut started on August 16 and ended on September 1. In 2020, measurements of GEM, GOM, and PHg started on July 17 and ended on August 4. GEM was analyzed on a 5-minute time resolution by a Tekran 2537A vapor phase analyzer at a flow rate of 1 L min^{-1}. This technique is based on the pre-concentration of GEM on dual gold cartridges followed by thermal desorption in a stream of argon gas and detection by cold vapor atomic fluorescence spectroscopy (CVAFS) at a wavelength of 253.7 nm. Skov et al. (2004) determined a detection limit of 0.1 ng m^{-3} and a reproducibility of 20 %, at a 95% confidence interval (CI) and above 0.5 ng m^{-3}. The instrument was manually calibrated with injections of a known amount of mercury before and after the campaigns and auto-calibrated in the field every 25th hour by an internal permeation source.

GOM and PHg were collected using a Tekran 1130 and 1135 speciation unit, respectively, upstream of the GEM analyzer, at a flow rate of 10 L min^{-1}. GOM was sampled onto potassium chloride (KCl) coated denuders. After sample collection, the denuders were flushed in a stream of zero air supplied from the 1130 pump module, then heated to 500°C during which GOM was thermally decomposed to GEM and detected by the Tekran 2537A analyzer. Denuders were exchanged weekly. PHg was sampled onto quartz filters, thermally released in a stream of zero air at 800 °C, and pyrolyzed on quartz chips also at 800 °C (for details about denuder and quartz filter performance and coating procedure, see Landis et al. (2002)). The cutoff size for PHg was < 2.5 μm. For the 2019 campaign, the sampling time was 80 minutes, while for the 2020 campaign the sampling time was 60 minutes. Due to technical issues during the 2019 campaign, measurements of PHg were not available. The limit of detection (LOD) for both GOM and PHg was calculated as three times the standard deviation (s.d.) of blanks values for the flush cycles, excluding the first measurement in a flush cycle as the heated sampling line still contains ambient air. The LODs for the 2019 and 2020 campaigns were 0.18 and 0.684 pg m^{-3}, respectively.

Atmospheric
Chemistry
and Physics
Discussions

2.3 Ancillary measurements

Meteorological parameters including wind speed, wind direction, air temperature, relative humidity, radiation, and snow depth were measured at Villum on a time resolution of 5 minutes. Ozone (O_3) was measured at Villum using a photometric O_3 analyzer (API M400) at 1 Hz, averaged to 30-minute means. The detection limit was 1 parts per billion by volume (ppbv),

130 with an uncertainty of 3% for measured concentrations above 10 ppbv and 6% below, respectively, on a 95% CI (Nguyen et al., 2016). All measurements used in this study were averaged (median) to correspond temporally to GOM and PHg sampling intervals.

2.4 Particle number size distribution and black carbon

Particle number size distributions (PNSD) from 0.3 to 10 μm were measured using an optical particle sizer (OPS, TSI 3330)

135 on a 10-minute time resolution. This size range is representative of coarse mode particles and a fraction of accumulation mode particles. The entire particle size spectrum was integrated to give the coarse mode particle number concentration (N_{Coarse}). The OPS was located at Villum and the data were vigorously quality controlled for abnormal instrument diagnostic parameters (RH and temperature) and the influence of local pollution (i.e., vehicles and activities from Station Nord).

Black carbon (BC) concentrations were measured using a MAGEE AE33 aethalometer (Drinovec et al., 2015) at a 1-
140 minute time resolution. The instrument is an absorption photometer that continuously collects aerosol particles onto a filter and measures light absorption from the resulting filter spot containing the aerosol. The AE33 automatically corrects for filter-loading effects by measuring absorption on a reference filter and operates at seven wavelengths: λ = 370, 470, 520, 590, 660, 880, and 950 nm. By using a standard BC mass absorption cross-section (MAC) of 7.77 m^2 g^{-1} at 880 nm, these absorption coefficients are converted to equivalent black carbon (eBC) mass concentrations. It has been found that the aethalometer
145 overestimates BC concentrations at Arctic sites compared to co-located absorption photometers (Backman et al., 2017). To account for this, an Arctic harmonization factor was used, adapted from Backman et al. (2017) to suit the newer aethalometer model. This has been widely used for Arctic datasets (Schmeisser et al., 2018; Zanatta et al., 2018; Schacht et al., 2019). Substantial uncertainties may arise from cross-sensitivity to scattering in the instrument, especially for Arctic aerosols, which are typically highly scattering. This uncertainty is estimated to be around 15% at Villum, using typical values of single
150 scattering albedo (SSA) and previously determined uncertainty studies (Weingartner et al., 2003; Drinovec et al., 2015).

2.5 Air mass history analysis

Air mass history was interrogated by use of the HYSPLIT trajectory model (Draxler and Hess, 1998; Rolph et al., 2017). Air mass back-trajectories of 120-hour length were calculated arriving at 50 m above ground level for every hour during the two campaigns. The trajectory starting height of 50 m was selected as a compromise between capturing air masses that are
155 representative of our sampling site and avoiding trajectories intercepting the surface, which can produce unrepresentative trajectories (Stohl, 1998); trajectories were also initialized at 20 m, which produced similar trajectory paths but often

Atmospheric
Chemistry
and Physics
Discussions

intercepted the surface. The trajectory length of 120 hours was selected to produce accurate trajectories but also capture the lifetime of GOM in the atmosphere. Global Data Assimilation System (GDAS) meteorological data on a 1° spatial resolution, employing modeled vertical velocity, were used as input for the model. The HYSPLIT model output included meteorological

160 variables along the trajectory path including relative humidity, precipitation, mixed layer height, and H_2O mixing ratio. These parameters along with sea ice concentrations and active fire data were utilized to inspect the geo-physical history of air masses arriving at Villum during the campaign periods (Greene et al., 2017; Greene, 2020). Daily polar gridded sea ice concentrations for the measurement period were obtained through the Nimbus-7 SMMR and DMSP SSM/I-SSMIS Passive Microwave Data from the National Snow and Ice Data Center (NSIDC) (Cavalieri et al., 1996). Fire data were provided by NASA's Fire

165 Information for Resource Management System (FIRMS), active fire data from NASA's Moderate Resolution Imaging Spectroradiometer (MODIS), and NASA's Visible Infrared Imaging Radiometer Suite (VIIRS) (Schroeder et al., 2014).

3 Results & Discussion

3.1 Atmospheric mercury and ground-level meteorological parameters

From the two campaigns, five events of enhanced GOM concentrations were observed: two during the 2019 campaign and

170 three during the 2020 campaign. These events were identified by enhancements of GOM over background levels. Results from the 2019 campaign, describing the time series of meteorological parameters and atmospheric mercury concentrations, are presented in Fig. 1. Wind direction, wind speed, and snow depth are displayed in Fig. S1. From Fig. 1, there are two distinct GOM enhancement events during the 2019 campaign: Event 1 from August 20 at 17:45 to August 27 at 00:10, and Event 2 from August 29 at 20:10 to September 1 at 18:20.

175 During the first days of Event 1 (August 21 and 22), GEM increased slightly from ~1.6 to ~1.7 ng m^{-3}. On the night of August 22, GEM suddenly dropped followed by a slow decrease until the afternoon of August 24 when it precipitously decreased, reaching a minimum of 1.1 ng m^{-3} on the morning of August 25. GEM then quickly increased back to consistent levels of ~1.5 ng m^{-3} for the remainder of the measurement campaign including Event 2. For Event 1, GOM gradually increased from zero on the afternoon of August 20 to the night of August 24, with the highest value (9.8 pg m^{-3}) on August 25. On the

180 night of August 25 and into the morning of August 26, GOM quickly decreased from ~8 pg m^{-3} to zero, corresponding to a concurrent increase in RH. As RH then decreased throughout the day of August 26, GOM once again increased to levels similar to those observed on the previous day. A back-trajectory analysis revealed that air masses arriving on August 26 had significant surface contact (Fig. S2). From August 27 to the evening of August 29, GOM is undetectable, before averaging (median ± m.a.d.) 2.8 ± 1.3 pg m^{-3} for Event 2, which started on August 29 and ended on September 1. Concerning the meteorological

185 parameters for Events 1 and 2, the wind direction was mainly from the southwest, with low but variable wind speed (4.9 ± 2.9 m s^{-1}). The relative humidity was low (< 90 % RH), averaging 63 ± 5 % RH for the two event periods. The temperature was routinely above freezing (2.1 ± 0.8 °C). The skies were clear with peak solar radiation above 200 W m^{-2}. Between the enhancement event periods and non-event periods of the 2019 campaign, temperature, relative humidity, wind direction, solar
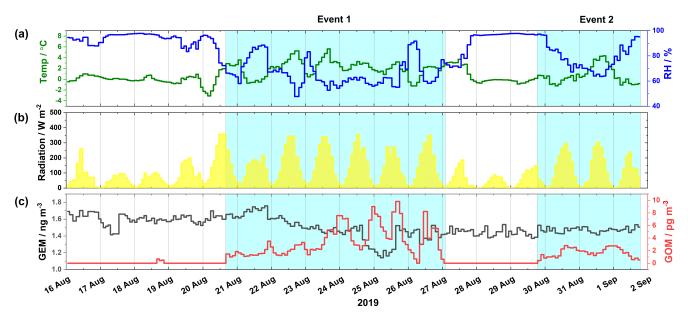
Atmospheric
Chemistry
and Physics
Discussions

radiation, GEM, and GOM were significantly different (Wilcoxon Rank Sum Test, 95 % CI); however, there was no significant

190   difference for wind speed.

Figure. 1. Overview of mercury and meteorological parameter measured during the 2019 campaign including **(a)** temperature (°C) in green on the left axis and relative humidity (%) in blue on the right axis, **(b)** radiation (W m^{-2}), and **(c)** GEM (ng m^{-3})

195   in black on the left axis and GOM (pg m^{-3}) in red on the right axis. The areas shaded in blue indicate Events 1 and 2.

Results from the 2020 campaign, describing the time series of atmospheric mercury species and meteorological parameters, are presented in Fig. 2. Wind direction, wind speed, and snow depth are displayed in Fig. S3. From Fig. 2, three distinct GOM enhancement events are observed: Event 3 from July 22 at 16:35 to July 23 at 13:15, Event 4 from July 24 at

200   11:55 to July 26 at 13:15, and Event 5 from July 30 at 17:00 to August 4 at 09:40. The 2020 campaign experienced higher GEM concentrations compared to the 2019 campaign. For example, GEM increased from ~1.7 ng m^{-3} on July 17 to ~2.8 ng m^{-3} on July 19, only to dip to ~1.7 ng m^{-3} on July 21 before increasing to ~2.4 ng m^{-3}. These elevated concentrations could be the result of oceanic evasion through open leads and fissures in the consolidated pack ice (Aspmo et al., 2006; DiMento et al., 2019), as air masses experienced extensive surface contact with sea ice on July 19–21 (Fig. S4a–c). For Event 3, GEM and

205   GOM averaged 1.7 ± 0.1 ng m^{-3} and 35.1 ± 13.9 pg m^{-3}, respectively. At the beginning of Event 3, GEM dropped from 2.1 to 1.5 ng m^{-3}, while GOM increased from 6.2 to 61.8 pg m^{-3}. For Event 4, GEM and GOM averaged 1.8 ± 0.1 ng m^{-3} and 8.7 ± 2.4 pg m^{-3}, respectively. During Event 4, GOM peaked at ~14 pg m^{-3} on July 24 at 13:55 and July 25 at 18:35, while GEM decreased from ~1.9 ng m^{-3} to ~1.4 ng m^{-3} before returning to levels of ~1.9 ng m^{-3} by the end of Event 4. For Event 5, GEM and GOM averaged 1.5 ± 0.03 ng m^{-3} and 9.8 ± 2.7 pg m^{-3}, respectively. At the beginning of Event 5, GEM was elevated at
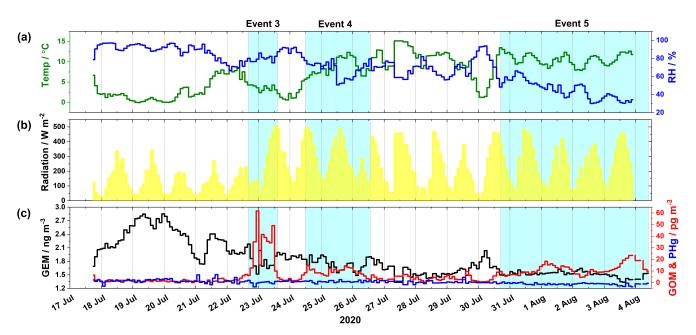
210 ~1.8 ng m^{-3} although quickly decreased to ~1.4 ng m^{-3} while GOM increased from near-zero values to enhanced concentrations of 20 pg m^{-3} for the remainder of Event 5. For Events 3, 4, and 5, PHg displayed no visible pattern and was constantly near or below LOD.

Meteorological parameters during the 2020 campaign are displayed in Fig. 2. Event 3 experienced decreasing temperatures (5 to 1 °C) and increasing RH (77 to 92 %) while Event 4 displayed an opposite pattern of increasing temperatures

215 (5 to 7, maximum 12 °C) and decreasing RH (77 to 79, minimum 52 %). For Events 3 and 4, the wind direction was mainly from the east with low and stable wind speeds (Fig. S2). For Event 5, the temperature exhibited a diurnal pattern (10.6 ± 1.2 °C) with low (< 70 %) and decreasing RH (minimum 30 %), the wind direction was consistently from the southwest with high wind speeds (median 8.8 m s^{-1}, max 12 m s^{-1}). During all three events, snow cover was near zero (Fig. S2) and global radiation was high during all three events (except during the beginning of Event 3, Fig 2). Between the enhancement event periods and

220 non-event periods of the 2020 campaign, temperature, relative humidity, wind speed, wind direction, solar radiation, GEM, and GOM were significantly different (Wilcoxon Rank Sum Test, 95% CI).

Figure. 2. Overview of mercury and meteorological parameters during the 2020 campaign including **(a)** temperature (°C) in

225 green on the left axis and relative humidity (%) in blue on the right axis, **(b)** radiation (W m^{-2}) shaded in yellow, and **(c)** GEM (ng m^{-3}) in black on the left axis, GOM (pg m^{-3}) in red on the right axis, and PHg (pg m^{-3}) in blue on the right axis. The area shaded in blue indicates Events 3, 4, and 5, respectively.

For Events 1, 2, 4, and 5, the ground level meteorological parameters mainly associated with GOM enhancement are

230 high levels of radiation and low RH. Interestingly, these events were not linked to cold temperatures, which has been previously

demonstrated to be associated with mercury oxidation (Ariya et al., 2015; Steffen et al., 2015). The stability of the Hg-Br intermediate is highly temperature-dependent (Goodsite et al., 2004, 2012). The temperature at Villum ranged from -3.1 to 5.6 °C and from 0.0 to 15.1 °C during the 2019 and 2020 campaign, respectively. Therefore, the ground-level temperatures are likely too high for local in situ production of GOM in the boundary layer to occur. This observation prompted the analysis of

235 air mass back-trajectories with arriving at Villum, and their meteorological data, to investigate the dynamics of GOM during these enhancement events.

3.2 Air mass history

Analysis of air mass history including both the trajectories and the associated meteorology along the paths can provide useful information regarding the source regions and favorable conditions for GOM formation and removal. Contour plots for different

240 meteorological parameters (temperature, relative humidity, solar radiation) and altitude for each trajectory along with GOM concentrations for the 2019 and 2020 campaigns are displayed in Fig. 3 and 4, respectively. Other meteorological parameters (H_2O mixing ratio and precipitation) for the 2019 and 2020 campaigns are shown in Fig. S5a–b and Fig. S5c–d, respectively.
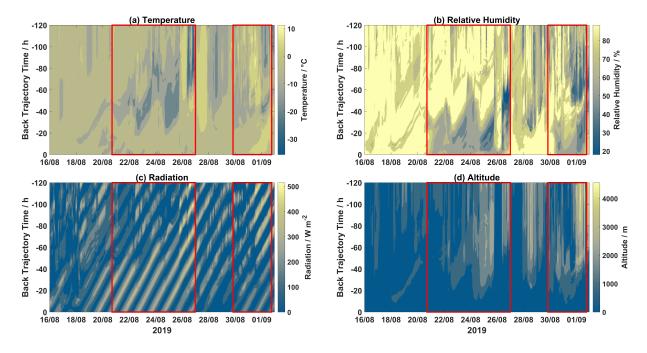

245 **Figure 3.** Contour plots of trajectory derived meteorological parameters **(a)** temperature, **(b)** relative humidity, **(c)** solar radiation, and **(d)** altitude, along each trajectory for the 2019 campaign. Event periods are outlined in red. The x-axis displays arrival time at Villum, the y-axis displays hours backward in time for each trajectory, and the color bar represents the meteorological parameter. Trajectories were producing via the HYSPLIT model.

Atmospheric
Chemistry
and Physics
Discussions

In 2019, air masses arriving during Events 1 and 2 were, on average, colder (temperature: -2.8 ± 3.2 °C), dryer (RH:

250   80 ± 15 %, accumulated precipitation: 3.8 ± 2.5 mm, and H_2O mixing ratio: 2.6 ± 0.7 g / $kg_{dry\ air}$), and exposed to more intense solar radiation (110 ± 73 W m^{-2}) when compared to non-event periods (temperature -1.1 ± 1.5 °C, RH: 90 ± 7 %, accumulated precipitation: 5.1 ± 3.0 mm, H_2O mixing ratio: 3.2 ± 0.4 g / $kg_{dry\ air}$, solar radiation: 100 ± 54 W m^{-2}). Trajectory temperature, RH, precipitation, H_2O mixing ratio, solar radiation, and altitude were significantly different (Wilcoxon Rank Sum Test, 95% CI) between GOM enhancement event periods and non-event periods during the 2019 campaign. For the 2020 campaign, a

255   similar pattern is observed for Events 3, 4, and 5 with air masses being, on average, colder (temperature: 0.4 ± 4.1 °C), drier (RH: 74 ± 17 %, accumulated precipitation: 1.9 ± 1.6 mm, and H_2O mixing ratio: 3.1 ± 0.7 g / $kg_{dry\ air}$) and exposed to more intense solar radiation (214 ± 104 W m^{-2}) when compared to non-event periods (temperature 1.3 ± 2 °C, RH: 91 ± 8 %, accumulated precipitation: 7.0 ± 3.6 mm, H_2O mixing ratio: 3.9 ± 0.6 g / $kg_{dry\ air}$, and solar radiation: 167 ± 85 W m^{-2}). During the 2020 campaign, trajectory temperature, RH, H_2O mixing ratio, solar radiation, and altitude were significantly different

260   (Wilcoxon Rank Sum Test, 95% CI) between GOM enhancement event periods and non-event periods. Higher levels of solar radiation enable the photolysis of reactive halogen species and lower relative humidity inhibits the partitioning of GOM into the liquid phase (Laurier, 2003; Soerensen et al., 2010; Brooks et al., 2011; Steen et al., 2011). Lower temperatures aid in the formation of GOM from HgBr; Skov et al. (2004) and Christensen et al. (2004) modeled a surface temperature below -4 °C for mercury depletion to occur in the Arctic, while Brooks et al. (2011) observed a temperature threshold of -15 °C for mercury

265   oxidation to occur. Therefore, it appears that while ground-level measurements showed no robust connection to cold temperatures, meteorological conditions along the trajectory path showed a relationship between GOM and subfreezing temperatures as well as dry, sunlit conditions.
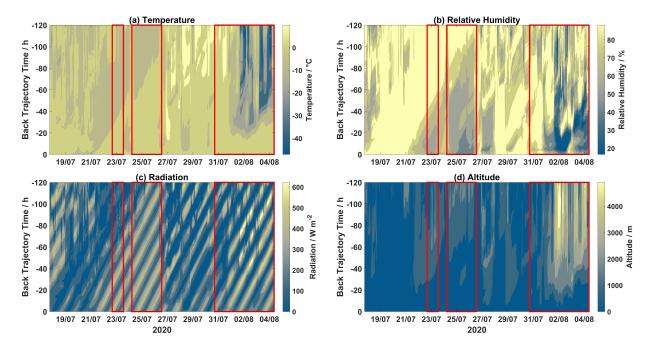
270

Figure 4. Contour plots of trajectory derived meteorological parameters **(a)** temperature, **(b)** relative humidity, **(c)** solar radiation, and **(d)** altitude, along each trajectory for the 2020 campaign. Event periods are outlined in red. The x-axis displays arrival time at Villum, the y-axis displays hours backward in time for each trajectory, and the color bar represents the meteorological parameter. Trajectories were producing via the HYSPLIT model.

The differences between ground-level and trajectory-derived meteorological parameters during enhancement events and non-events imply that these air masses are likely decoupled from the boundary layer. To examine the vertical origin of these air masses, an analysis of the altitude of trajectories arriving at Villum was performed. Figures 3d and 4d display a contour plot of the altitude for each hourly back-trajectory for the 2019 and 2020 campaign, respectively. From these figures, it is evident that during GOM enhancement events air masses spent considerable time aloft before arrival at Villum. For the 2019 campaign, median back-trajectory altitudes during event periods were 754 ± 467 m, compared to 371 ± 351 m during non-event periods. For the 2020 campaign, median altitudes during event periods were 1075 ± 578 m, compared to 425 ± 352 m during non-event periods. Indeed, air masses that arrived during event periods were above the mixed layer height 90 and 99 % of the time in the 2019 and 2020 campaigns, respectively. Air masses that arrived during non-event periods were above the mixed layer height only 64 and 82 % of the time in the 2019 and 2020 campaigns, respectively. Together, the analysis of air mass history demonstrates that the origin of the GOM enhancement events is the free troposphere under favorable meteorological conditions (cold and dry with intense solar radiation along the trajectory path).

Interestingly, during event periods, air masses experienced these favorable conditions at different times during transport; temperatures were colder further back along the trajectory path while RH was lower closer to the measurement site

11

Atmospheric
Chemistry
and Physics
Discussions

(Fig. 3 and 4). During the 2019 campaign, minimum temperatures were observed, on average (median), 48 hours before arrival, while minimum RH was observed 23 hours before arrival. These times correspond to average altitudes of 1538 m and 427 m, for minimum temperature and RH, respectively. During the 2020 campaign, temperatures were, on average, at a minimum 76 hours before arrival, while RH was at a minimum 16 hours before arrival. These times correspond to average altitudes of 1795

295 m and 542 m, for minimum temperature and RH, respectively. These findings highlight the complex relationship between GOM formation, removal, and meteorological parameters during transport. Colder temperatures in the free troposphere are likely facilitating the formation of GOM, by increasing the stability of the Hg^I intermediate at colder temperatures, while low RHs closer to the surface are limiting uptake of GOM into the aqueous phase. Additionally, given the low surface resistance of GOM over snowpack (Skov et al., 2006), dry (and possibly wet) deposition will increase occur when air masses come in

300 close contact with the surface, resulting in decreased concentrations. Thus, it appears the formation of GOM is facilitated in the free troposphere and the survival is governed closer to the surface.
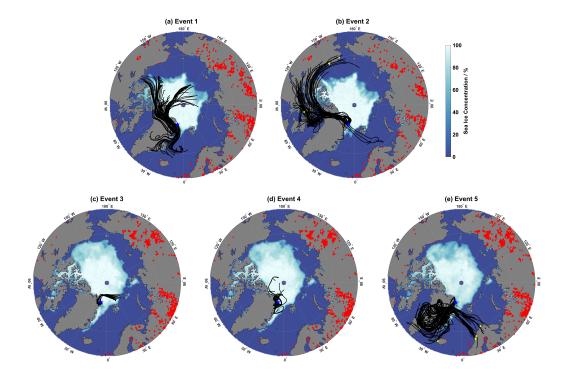

305 **Figure. 5.** Map of air mass back-trajectories during Events 1–5 in **(a)** through **(e)**. Individual hourly trajectories are in black, active fires during each event are in red, active fires intersecting trajectories within 1° latitude/longitude and within 1 hour are in yellow (active fires from the previous 5 days before the start of an event were included to reflect the trajectory length), and sea ice concentration is given by the color bar. The position of Villum is marked by the blue star. Trajectories were producing via the HYSPLIT model. Sea ice concentration was taken from NSIDC. Fire data were obtained from the FIRMS database.

310

Geospatially, the GOM enhancement events show different source regions. Figure 5a–e shows hourly air mass back-trajectories, combined with sea ice concentrations and active fire data, for each event. To capture the presence of fires in relation to the length of each trajectory, active fires from the previous 5 days before the start of each event and up to the end of each event were included. For Event 1, air masses showed two main source regions: the first is the Arctic with air masses

315 originating from either the central Arctic Ocean or the northern part of the Canadian archipelago and passing over Northern Greenland, and the other is the Northern Atlantic. Event 2 showed a major contribution of air masses from the Canadian archipelago with smaller contributions from the Northern Atlantic just south of Svalbard. Events 3 and 4 showed air masses originating from the Arctic Ocean with little spatial extent. Event 5 showed the largest spatial extent, with air masses arriving from mainly over the Greenlandic Ice Sheet, although contributions were also found from the Northern Atlantic and parts of

320 Northern Scandinavia. Other than Events 3 and 4, the geospatial origins of air masses during GOM enhancement events were quite diverse. Events 3 and 4 were only separated by a couple of hours and therefore similar air mass origin is expected for the two events. Figure 5a–e shows that the air mass origins during GOM enhancement events are heterogeneously distributed throughout the Arctic as well as the Canadian Archipelago and Scandinavia.

3.3 Comparison with mid-latitude studies

325 Previous studies have demonstrated the influence of the troposphere on mercury concentrations. In the mid-latitudes of the northern hemisphere, the free troposphere has been established as a source of GOM through modeling studies (Gratz et al., 2015; Shah and Jaeglé, 2017) and observations from both aircraft campaigns (Talbot et al., 2007; Gratz et al., 2015) and high altitude sites (Swartzendruber et al., 2006; Faïn et al., 2009; Fu et al., 2016). Depletions of GEM were observed onboard research flights in the upper troposphere (8–12 km) during the INTEX-B campaign in 2006 over the North Pacific (Talbot et

330 al., 2007). GEM was rarely detected when ozone was greater than 300 ppb; the authors ascribed this relationship as an indicator of time spent in the stratosphere. They hypothesized that the near-ppm levels of ozone in the stratosphere were the cause of the depleted GEM. Faïn et al. (2009) reported similar observations of the free troposphere acting as a source of oxidized mercury at a high elevation site (3220 m above sea level) in the Rocky Mountains, USA. They also observed that the presence of GOM was dependent on RH. They hypothesized that the build-up of GOM in the free troposphere was governed exclusively

335 by the existence of low RH, possibly due to the lack of scavenging by particles at low RH levels. Modeling studies have also shown the troposphere to be a source of GOM. Using the GEOS-Chem global chemical transport model, Holmes et al. (2006) and Holmes et al. (2010) identified Br to be the dominant oxidant of GEM globally, with most of the oxidation occurring in the middle and upper troposphere. Shah and Jaeglé (2017) arrived at a similar conclusion using GEOS-Chem that much of the mercury oxidation by Br occurs in the middle and upper troposphere. These studies show the free troposphere to be a source

340 of GOM in the mid-latitudes, however, there are a limited number of field studies on GOM in the High Arctic summer and none, to the authors' knowledge, on the influence of the free troposphere on GOM levels. Similar chemistry is likely the cause of the observations in this study; however, the Arctic atmosphere is largely separated from the mid-latitudes during summer

on account of contraction of the polar dome, so there may be differences in the dynamics, albeit unlikely (Holmes et al., 2010). This study provides field validation of these previous modeling studies from the mid-latitudes by identifying the free

345 troposphere as a source of GOM in the High Arctic summer.

3.4 Ozone

Given the source of the enhanced GOM concentrations was identified to be the cold, dry free troposphere, our analysis now turns to other atmospheric constituents, particularly ozone. An analysis of ground-level ozone measurements can help to provide insight into the dynamics of GOM as mercury depletion events and ozone depletion events often occur concurrently

350 through reactions with halogen species.

GEM and GOM concentrations along with ozone mixing ratios for the 2019 and 2020 campaigns are displayed in Fig. 6a and Fig. 6d, respectively. During non-event periods in the 2019 campaign, ozone is either low or decreasing. During Event 1, ozone increases concurrently with GOM, when they both peak on August 25 at 45.5 ppb and 9.8 pg m^{-3} for ozone and GOM, respectively, while GEM exhibits a minimum on August 25 at 1.1 ng m^{-3} (Fig. 6a). For Event 1, ozone averaged 36.9

355 $\pm$ 4.7 ppb. The peak ozone level is abnormally high for the late summer (median $\pm$ m.a.d. ozone mixing ratio for August 2010–2018 is 24.6 $\pm$ 3.1 ppb). Ozone then decreases during the second non-event period and only increases again during Event 2 to an average of 31.9 $\pm$ 2.6 ppb.

For the 2020 campaign, a similar relationship between ozone and GOM is observed (Fig. 6d). During Event 3, ozone is increasing simultaneously with GOM while GEM is decreasing; for this event, ozone averaged 26.7 $\pm$ 0.8 ppb. For Event 4,

360 ozone averaged 25.3 $\pm$ 1.6 ppb and is at background levels for much of the event. On July 25, ozone peaked at 34 ppb before returning to background levels. For the non-event period from July 26 to 30, ozone is significantly elevated over background levels, although there is an absence of enhanced GOM concentrations. This discrepancy can again be accounted for by the meteorological conditions along the trajectory path (Fig. 4 and S3); elevated temperature, RH, precipitation, and H$_2$O mixing ratios lead to the removal of GOM, while ozone is only slightly water-soluble leading to less efficient wet removal (Sander,

365 2015). For Event 5, ozone follows a similar pattern as GOM, increasing at the beginning of the event and remaining elevated for the duration. Event 5 experienced the highest average trajectory altitudes (1530 $\pm$ 813 m) as well as highest average ozone mixing ratios (30.7 $\pm$ 1.7 ppb), which were elevated over normal levels during July (median $\pm$ m.a.d. ozone mixing ratio for August 2010–2018 is 23.6 $\pm$ 2.8 ppb).

For the GOM enhancement events in 2019, there is a moderate negative correlation between GEM and ozone

370 (Spearman's rank coefficient -0.62, Fig. 6b), as well as a moderate positive correlation between GOM and ozone (Spearman's rank coefficient 0.71, Fig. 6c). For the 2020 campaign, this moderate negative relationship between GEM and ozone is retained (Spearman's rank coefficient -0.72, Fig. 6e), although for GOM and ozone the correlation is moderate to weak (Spearman's rank coefficient 0.45, Fig. 6c). This is likely due to the high concentrations observed during Event 3, when removing this event from the correlation analysis for the 2020 campaign, the Spearman's rank coefficient increases to 0.62. These relationships

375 cast doubt on the boundary layer production of GOM, analogous to the mechanisms of AMDEs. During AMDEs, ozone and

GEM are positively correlated due to mutual reaction with halogen species and are both extremely depleted due to strong halogen explosion events (Schroeder et al., 1998; Lindberg et al., 2002; Berg et al., 2003; Skov et al., 2004; Brooks et al., 2006; Simpson et al., 2015). While ozone mixing ratios were high during GOM enhancement events, they are an order of magnitude below levels reported in the upper troposphere/lower stratosphere (Talbot et al., 2007), and given the slow rate

380   reaction coefficient (Pal and Ariya, 2004), ozone is an improbable oxidant of mercury during these campaigns. Any depletions of ozone during GEM oxidation is likely masked by the elevated levels of ozone in the free troposphere.
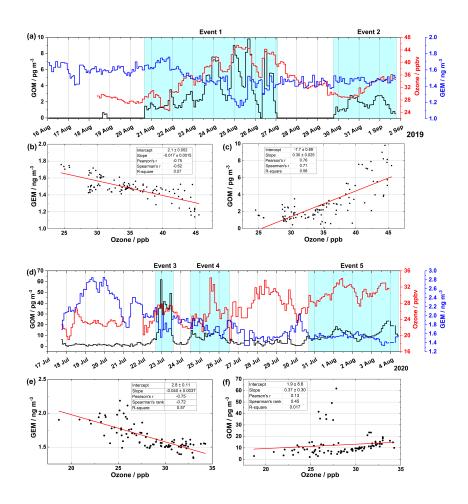

Figure. 6. Time series of GOM concentrations (pg m^{-3}) in black on the left axis, ozone mixing ratios (ppbv) in red on the first

385   right axis, and GEM concentrations (ng m^{-3}) in blue on the second right axis for **(a)** the 2019 and **(d)** the 2020 campaign. Correlation between GEM and ozone for **(b)** the 2019 and **(e)** the 2020 campaign. Correlation between GOM and ozone for **(c)** the 2019 campaign and **(f)** the 2020 campaign. The areas shaded in blue indicate events periods. Correlations were calculated using the event periods. The slopes for **(b)**, **(c)**, **(e)**, and **(f)** are significantly different from zero at the 95 % CI.

15

390   The relationship between GOM and ozone suggests a common source or source regions for these two species. Sources of ozone in the High Arctic include transport from mid-latitudes, local production from NO_x present in the snowpack, peroxyacetyl nitrate (PAN) photolysis, and intrusion from the free troposphere/stratosphere (Dibb et al., 2002; Walker et al., 2012; Law et al., 2014). During the winter and spring, transport from the mid-latitudes (Hirdman et al., 2009) and the free troposphere/stratosphere (Semane et al., 2007; Arnold et al., 2015) are dominant ozone sources. During the summer and

395   autumn, contraction of the polar dome decreases transport of ozone and its precursors (e.g., CO, PAN, NO_x) from the mid-latitudes, making intrusion from the free troposphere/stratosphere a more dominant source of ozone. Elevated ozone mixing ratios have been observed with increasing altitude in the Arctic during the ARCTAS aircraft campaigns (Jacob et al., 2010; Monks et al., 2015). Conversely, increased photochemical activity and deposition are important sinks for ozone at the ground level during the summer (Helmig et al., 2007; Arnold et al., 2015). Enhancements of GOM, which exhibited a positive

400   correlation with ozone, have also been observed during subsidence events on Antarctica (Brooks et al., 2008; Pfaffhuber et al., 2012). Therefore, the elevated ozone levels during GOM enhancement events and positive correlation between these two species are an indicator of influence from air masses in the free troposphere, strengthening our hypothesis of the free troposphere as the source of GOM during summer (Sect. 2.2).

3.5 Particle number and black carbon

405   Our attention now turns to other atmospheric constituents, namely aerosol particles and black carbon content. The free troposphere has been shown to be a source of aerosol particles to the boundary layer in the Arctic (Igel et al., 2017) and contains elevated concentrations of BC over the surface level (Schulz et al., 2019). The presence of coarse mode aerosol particles has also been shown to be a necessary condition for observing BrO (a tracer for halogen activation) in the Arctic (Bognar et al., 2020). A common source of aerosol particles, black carbon, and mercury species is biomass burning (Friedli et

410   al., 2009; Soerensen et al., 2010; Winiger et al., 2019). Therefore, we analyzed these constituents to examine their interaction with GOM with respect to the different sources.

During the non-event periods of the 2019 campaign, the coarse mode particle number concentration (N_{Coarse}) and black carbon (BC) are both low, 0.5 ± 0.3 cm^{-3} and 1.2 ± 1.1 ng m^{-3}, respectively. For Event 1, N_{Coarse} and BC are both elevated (4.2 ± 3.1 cm^{-3} and 8.6 ± 6.0 ng m^{-3}, respectively) and increase concurrently with GOM, reaching a maximum concentration of ~11

415   cm^{-3} and ~26 ng m^{-3}, respectively, on August 25 (Fig. 7a). For Event 2, N_{Coarse} and BC returned to low values, although at a higher level compared to non-event periods, 2 ± 0.1 cm^{-3} and 3.8 ± 0.6 ng m^{-3}, respectively. This pattern is comparable to the behavior of ozone (Sect. 2.3, Fig. 6a). For the enhancement events during the 2019 campaign, there is a positive correlation for event periods between GOM and N_{Coarse} (Spearman's rank coefficient 0.71), as well as between GOM and BC (Spearman's rank coefficient 0.62). For the 2020 campaign, a different scenario is observed between N_{Coarse}, BC, and GOM (Fig. 7b). For

420   Events 3 and 4, there is a slight enhancement of N_{Coarse} and BC levels when compared to the preceding non-event periods (Fig. 7b). For Event 5, both N_{Coarse} and BC are decreasing and low, 0.6 ± 0.1 cm^{-3} and 2.8 ± 1.1 ng m^{-3}, respectively. For enhancement events during the 2020 campaign, GOM is not correlated with N_{Coarse} and BC (Spearman's rank coefficient -0.02 and -0.07,
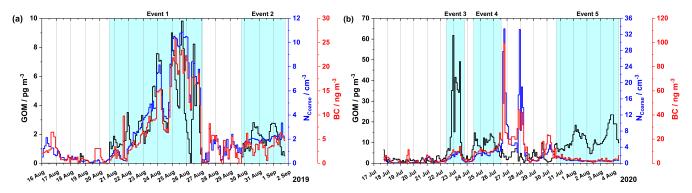
Atmospheric
Chemistry
and Physics
Discussions

respectively). Given the high concentrations during Event 3, these measurements may be skewing the results of the correlation analysis, however, if they are removed, the Spearman's rank coefficient between GOM and both N_{Coarse} and BC becomes

425   moderately negative (Spearman's rank -0.25 and -0.33, respectively). This moderate negative correlation is due to decreasing concentrations during Event 5. Air masses during this event arrived from high altitudes from over the Greenlandic ice sheet (Sect. 2.2), therefore the low concentrations of N_{Coarse} and BC are likely a representation of upper tropospheric air masses above the polar dome, which are extremely pristine (Schulz et al., 2019).

430

Figure. 7. Gaseous oxidized mercury (pg m^{-3}) in black on the left axis, coarse mode particle number concentration (cm^{-3}) in blue on the first right axis, and black carbon (ng m^{-3}) in red on the second right axis for **(a)** the 2019 and **(b)** the 2020 campaign. The areas shaded in blue indicate event periods.

435   Given the correlation between GOM, BC, and N_{Coarse} during enhancement events, biomass burning could be a potential source. To investigate the influence of biomass burning emission on GOM concentrations and the two episodes of high N_{Coarse} and BC concentrations during the 2020 campaign, active fire data from the FIRMS database were utilized in connection with air mass back-trajectory analysis for each event (active fires from the previous 5 days before the start of an event were included to reflect the trajectory length). As seen in Fig. 5a–e in Sect. 3.2, the geospatial origins of air masses during GOM enhancement

440   events are heterogeneously distributed. During the enhancement events, there are few intersections between air mass back-trajectories and active fires during Events 2 and 5 and none for Events 1, 3, and 4. GOM levels during Events 2 and 5 were low compared to other events (Fig. 1 and 2) and there is minimal intersection of back-trajectories and fires. Therefore, it appears that biomass burning and/or combustion related emissions have little to no influence on GOM levels observed at Villum.

445   During the 2020 campaign, there are two episodes, the first from July 26 at 15:15 to July 27 at 11:35 and the second from July 27 at 19:05 to July 28 at 09:05, where N_{Coarse} and BC are significantly elevated, reaching up to 33 cm^{-3} and 100 ng m^{-3}, respectively, compared to the rest of the campaign (Fig. 7b). These two episodes are observed during non-event periods (Fig. 7b). These episodes are likely long-range transported, as they are too gradual and long to be identified as local pollution from activities at Station Nord. Figure 8a and b show air mass back-trajectories for the first and second episodes, respectively,
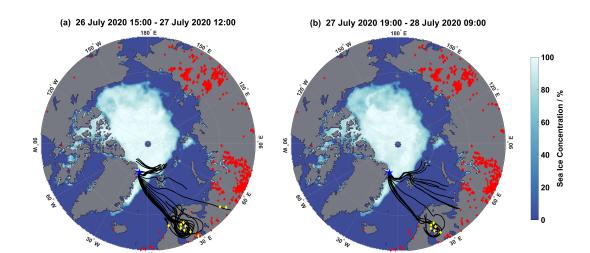
17

Atmospheric
Chemistry
and Physics
Discussions

450   combined with active fire data from the previous 5 days to the end of the episode. These episodes, which originate mainly

from Fennoscandia with smaller contributions from the Arctic Ocean and the Barents Sea, are influenced by biomass burning

emissions from active fires around the Bay of Bothnia (Fig. 8). GOM during these episodes is low, 2.6 ± 1.1 pg m^{-3} for the first

episode and 1.8 ± 0.9 pg m^{-3} for the second episode. This shows that while biomass burning emissions can influence the Arctic

atmospheric composition, they do not impact GOM concentrations.

455

Figure. 8. Map of air mass back-trajectories during **a)** the first episode and **b)** the second episode of elevated N$_{Coarse}$ and BC
concentrations. Individual hourly trajectories are in black, active fires during each event are in red, active fires intersecting
trajectories within 1° latitude/longitude and within 1 hour are in yellow (active fires from the previous 5 days before the start
460   of an episode were included to reflect the trajectory length), and sea ice concentration is given by the color bar. The position
of Villum is marked by the blue star. Trajectories were producing via the HYSPLIT model. Sea ice concentration was taken
from NSIDC. Fire data were obtained from the FIRMS database.

While these positive correlations between GOM and both N$_{Coarse}$ and BC appear not to be indicative of a common

465   source, they do suggest a common sink. A dominant sink for aerosol particles is scavenging by cloud droplets and removal via

wet deposition (Browse et al., 2012). Tunved et al. (2013) observed a decrease in particle mass and diameter with increased

accumulated precipitation at Ny Ålesund for the period 2000–2010, while Croft et al. (2016) used the GEOS-Chem-TOMAS

model to simulate the Arctic aerosol annual cycle and found coagulation scavenging of interstitial aerosols to be a strong

control on accumulation mode particles. Presuming that an RH greater than 95 % signifies air masses were within a cloud

470   (Freud et al., 2017), the time spent in-cloud could be calculated for each event. Air masses during Events 1 and 2 spent 23 and

12 % of the time in-cloud, respectively, and 20 % combined. For Events 3, 4, and 5, air masses spent 50 %, 8 %, and 16 % of

the time in-cloud, and 15 % combined. Interestingly, Event 3 exhibited both the highest GOM concentrations and the most

Atmospheric
Chemistry
and Physics
Discussions

time in-cloud, an observation for which we do not have an explanation thus far. While Event 3 followed the general pattern
displayed by the other events (cold, dry air from the free troposphere under sunlit conditions), there appears other factors
475   influencing the high concentrations of GOM during this event that we are unable to detect at this time. Overall, we hypothesize
that the lack of sinks in the free troposphere for accumulation mode particles and BC due to the absence of wet removal
processes and diminished water content is likely the reason for the observed increase in N_{Coarse} and BC during the enhancement
events. Furthermore, we did not find evidence of biomass burning emissions influencing GOM levels at Villum.

3.6 Possible halogen sources

480   With the source region of the observed GOM identified as the cold, dry free troposphere, what are the possible sources of
halogen species? Sources of these reactive halogen species include snowpack, sea ice, frost flowers, refreezing leads, sea-salt
aerosol, and liable halogen reservoir species (i.e., halocarbons and inorganic bromine) (Kaleschke et al., 2004; Brooks et al.,
2006; Simpson et al., 2015; Peterson et al., 2018). As demonstrated by Halfacre et al. (2019) and Burd et al. (2017), a frozen
heterogeneous surface is required for the propagation of halogen explosions. However, with the altitude and meteorological
485   conditions of back-trajectories indicating free tropospheric air masses (Sect. 3.2), as well as ground-level temperatures
regularly above 0 °C and little snow cover during both campaigns, emissions from snowpack, sea ice, and frost flowers appear
to be unlikely sources in this study.

Coarse mode particles and aerosol optical depth have been shown to be connected with BrO enhancement events
(Peterson et al., 2017; Bognar et al., 2020), through the recycling of halogens on sea salt aerosol surfaces in the troposphere.
490   Indeed, previous studies have found depletions of bromine in coarse mode particles in the polar regions (Giordano et al., 2018;
Hara et al., 2018; Frey et al., 2020). The positive correlation between GOM and N_{Coarse} observed during our study (Fig. 7),
could consequently be due to halogens being activated and recycled on coarse mode aerosol particle surfaces. As stated in
Sect. 3.5, we hypothesize instead that the positive correlation between GOM and N_{Coarse} is due to decreased sinks in the free
troposphere, although the contribution from halogen activation and recycling cannot be ruled out without high time resolution
495   measurements of aerosol chemical composition. While N_{Coarse} is low throughout both campaigns, coarse mode particles are
likely one of the few heterogeneous surfaces in the free troposphere, therefore, they could have a large impact on halogen
recycling.

One biogenic source of halogen species is the emission of halocarbons from marine emissions by micro-organisms,
e.g., macroalgae, ice algae, and phytoplankton (Sturges et al., 1992; Quack and Wallace, 2003). Thin, porous sea ice has been
500   shown to readily emit halocarbons during the Arctic summer (Atkinson et al., 2014), and our studies were conducted in July–
September when sea ice is at a minimum (Comiso, 2012). Once emitted from the ocean, these halocarbons are photolyzed in
the troposphere to produce reactive halogen species (Yang et al., 2005). In our study, the vertical extent of air mass back-
trajectories during enhancement events was consistently from aloft, under cold, dry, and sunlit conditions. The spatial extent
showed no consistent source regions, indicating that GEM oxidation is ubiquitous in the free troposphere of the High Arctic.
505   Given the vertical profile and spatial extent of air masses during enhancement events, biogenic emissions of halocarbons and

emissions of coarse mode aerosol particles from open waters and marginal ice zones would therefore represent a widespread source throughout the Arctic.

Therefore, we hypothesize that the oxidants responsible for the mercury oxidation result from the photolysis of short-lived halocarbons emitted from marine biological activity and were possibly sustained via recycling on aerosol surfaces.
510 However, this is a working hypothesis and further research is needed to confirm this theory, specifically column and in situ measurements of reactive halogen species, their precursors, aerosol chemical composition, and mercury species.

4 Summary and conclusion

While the behavior of GEM and GOM during the spring in the High Arctic has received much attention, the dynamics of GOM in the late summer/autumn have seldom been investigated. Therefore, we conducted measurements of GEM, GOM,
515 PHg (only 2020), meteorological parameters, ozone, and aerosol particle physical properties at Villum Research Station in Northeastern Greenland during the High Arctic summer in 2019 and 2020. By probing the air mass history during five GOM enhancement events, we show that enhancements of GOM are largely controlled by temperature, RH, and solar radiation. Analysis of air mass history provides direct evidence of influence from the free troposphere, while measurements of ozone, BC, and coarse mode particle number concentration support this conclusion. Biomass burning was not found to contribute to
520 GOM enhancement events, although it affects N_{Coarse} and BC concentrations through long-range transport. These measurements and analyses provide insight into the behavior of GOM during summer in the High Arctic and provide validation for previous studies from the mid-latitudes, where the free troposphere has been identified to be a source of GOM. The behavior of mercury in a changing Arctic climate is still an area with many knowledge gaps, and this work seeks to bridge those gaps, although further research (especially long-term, mercury speciation measurements) is needed.
525 With changing conditions in the Arctic (i.e., rising temperatures, melting sea ice, longer melt seasons), there is large uncertainty regarding the oxidation and deposition of mercury in response to these changes (Stern et al., 2012). For example, with the Arctic becoming warmer (Jiang et al., 2020) and therefore wetter, the feedback mechanisms on mercury oxidation remain an important scientific question. Warming temperatures will decrease the stability of the Hg^{I} intermediate and possibly increase biogenic production of halocarbons as well as increasing atmospheric water vapor, which will favor increased uptake
530 of oxidized mercury into the particulate phase and its removal by wet deposition. The magnitude of these contrasting effects and their consequences for GOM levels in the High Arctic is still an open question. Given the positive correlation between GOM and aerosol particles, and their role in halogen activation, changes in the size distribution and chemical composition of aerosol particles could have implications for mercury oxidation. Recent trends in declining sea ice (Stroeve et al., 2012) could increase the sea salt aerosol burden, thus potentially increasing mercury oxidation and deposition via increased halogen
535 recycling and particulate mercury deposition. Declining sea ice could also increase GEM evasion from the Arctic Ocean, shifting the Arctic Ocean from a sink to a source (Ariya et al., 2004; Dastoor and Durnford, 2014). Future studies addressing the contribution of the free troposphere to boundary layer GOM concentrations along with flux measurements of dry and wet

deposition of GOM in the summer will help answer these questions. The presented work aims to bridge some of the knowledge gaps in mercury processing although further research is needed to better understand how the behavior of atmospheric mercury will respond in a changing climate.

Data availability. All data used in this publication are available to the community and can be accessed by request to the corresponding author Jakob Boyd Pernov (jbp@envs.au.dk).

Author contributions. JBP, BJ, HSK designed the study. JBP and BJ performed the measurements. JBP performed all data analysis. HSK was the project leader. JBP wrote the manuscript with comments from all co-authors.

Competing interests. The authors declare that they have no conflict of interest.

Atmospheric
Chemistry
and Physics
Discussions

References

AMAP: Snow, water, ice and permafrost in the Arctic (SWIPA), Oslo: Arctic Monitoring and Assessment Programme (AMAP). 2011.

565 Angot, H., Dastoor, A., De Simone, F., Gårdfeldt, K., Gencarelli, C. N., Hedgecock, I. M., Langer, S., Magand, O., Mastromonaco, M. N., Nordstrøm, C., Pfaffhuber, K. A., Pirrone, N., Ryjkov, A., Selin, N. E., Skov, H., Song, S., Sprovieri, F., Steffen, A., Toyota, K., Travnikov, O., Yang, X., and Dommergue, A.: Chemical cycling and deposition of atmospheric mercury in polar regions: review of recent measurements and comparison with models, Atmos Chem Phys, 16, 10735-10763, 10.5194/acp-16-10735-2016, 2016.

570 Ariya, P. A., Dastroor, A. P., Amyot, M., Schroeder, W. H., Barrie, L., Anlauf, K., Raofie, F., Ryzhkov, A., Davignon, D., Lalonde, J., and Steffen, A.: The Arctic: a sink for mercury, Tellus B: Chemical and Physical Meteorology, 56, 397-403, 10.3402/tellusb.v56i5.16458, 2004.

Ariya, P. A., Amyot, M., Dastoor, A., Deeds, D., Feinberg, A., Kos, G., Poulain, A., Ryjkov, A., Semeniuk, K., Subir, M., and Toyota, K.: 575 Mercury physicochemical and biogeochemical transformation in the atmosphere and at atmospheric interfaces: a review and future directions, Chem Rev, 115, 3760-3802, 10.1021/cr500667e, 2015.

Arnold, S. R., Emmons, L. K., Monks, S. A., Law, K. S., Ridley, D. A., Turquety, S., Tilmes, S., Thomas, J. L., Bouarar, I., Flemming, J., Huijnen, V., Mao, J., Duncan, B. N., Steenrod, S., Yoshida, Y., Langner, J., and Long, Y.: Biomass burning influence on high-latitude tropospheric ozone and reactive nitrogen in summer 2008: a multi-model analysis based on POLMIP simulations, Atmos. 580 Chem. Phys., 15, 6047-6068, 10.5194/acp-15-6047-2015, 2015.

Aspmo, K., Temme, C., Berg, T., Ferrari, C., Gauchard, P. A., Fain, X., and Wibetoe, G.: Mercury in the atmosphere, snow and melt water ponds in the North Atlantic Ocean during Arctic summer, Environmental Science & Technology, 40, 4083-4089, 10.1021/es052117z, 2006.

585

Atkinson, H. M., Hughes, C., Shaw, M. J., Roscoe, H. K., Carpenter, L. J., and Liss, P. S.: Halocarbons associated with Arctic sea ice, Deep Sea Research Part I: Oceanographic Research Papers, 92, 162-175, https://doi.org/10.1016/j.dsr.2014.05.012, 2014.

Backman, J., Schmeisser, L., Virkkula, A., Ogren, J. A., Asmi, E., Starkweather, S., Sharma, S., Eleftheriadis, K., Uttal, T., Jefferson, A., 590 Bergin, M., Makshtas, A., Tunved, P., and Fiebig, M.: On Aethalometer measurement uncertainties and an instrument correction factor for the Arctic, Atmos. Meas. Tech., 10, 5039-5062, 10.5194/amt-10-5039-2017, 2017.

Berg, T., Sekkesæter, S., Steinnes, E., Valdal, A.-K., and Wibetoe, G.: Springtime depletion of mercury in the European Arctic as observed at Svalbard, Science of The Total Environment, 304, 43-51, https://doi.org/10.1016/S0048-9697(02)00555-7, 2003.

595

Bognar, K., Zhao, X., Strong, K., Chang, R. Y.-W., Frieß, U., Hayes, P. L., McClure-Begley, A., Morris, S., Tremblay, S., and Vicente-Luis, A.: Measurements of Tropospheric Bromine Monoxide Over Four Halogen Activation Seasons in the Canadian High Arctic, Journal of Geophysical Research: Atmospheres, 125, e2020JD033015, 10.1029/2020jd033015, 2020.

600 Brooks, S., Arimoto, R., Lindberg, S., and Southworth, G.: Antarctic polar plateau snow surface conversion of deposited oxidized mercury to gaseous elemental mercury with fractional long-term burial, Atmospheric Environment, 42, 2877-2884, https://doi.org/10.1016/j.atmosenv.2007.05.029, 2008.

Brooks, S., Moore, C., Lew, D., Lefer, B., Huey, G., and Tanner, D.: Temperature and sunlight controls of mercury oxidation and deposition 605 atop the Greenland ice sheet, Atmos Chem Phys, 11, 8295-8306, 10.5194/acp-11-8295-2011, 2011.

Brooks, S. B., Saiz-Lopez, A., Skov, H., Lindberg, S. E., Plane, J. M. C., and Goodsite, M. E.: The mass balance of mercury in the springtime arctic environment, Geophysical Research Letters, 33, 10.1029/2005gl025525, 2006.

610 Browse, J., Carslaw, K. S., Arnold, S. R., Pringle, K., and Boucher, O.: The scavenging processes controlling the seasonal cycle in Arctic sulphate and black carbon aerosol, Atmos. Chem. Phys., 12, 6775-6798, 10.5194/acp-12-6775-2012, 2012.

Burd, J. A., Peterson, P. K., Nghiem, S. V., Perovich, D. K., and Simpson, W. R.: Snowmelt onset hinders bromine monoxide heterogeneous recycling in the Arctic, Journal of Geophysical Research: Atmospheres, 122, 8297-8309, 10.1002/2017jd026906, 2017.

615

Atmospheric
Chemistry
and Physics

Discussions

Cavalieri, D. J., Parkinson, C. L., Gloersen, P., and Zwally, H. J.: Sea Ice Concentrations from Nimbus-7 SMMR and DMSP SSM/I-SSMIS Passive Microwave Data, Version 1., https://doi.org/10.5067/8GQ8LZQVL0VL. , 1996.

620   Christensen, J. H., Brandt, J., Frohn, L. M., and Skov, H.: Modelling of Mercury in the Arctic with the Danish Eulerian Hemispheric Model, Atmos. Chem. Phys., 4, 2251-2257, 10.5194/acp-4-2251-2004, 2004.

Comiso, J. C.: Large Decadal Decline of the Arctic Multiyear Ice Cover, Journal of Climate, 25, 1176-1193, 10.1175/jcli-d-11-00113.1, 2012.

625   Croft, B., Martin, R. V., Leaitch, W. R., Tunved, P., Breider, T. J., amp, apos, Andrea, S. D., and Pierce, J. R.: Processes controlling the annual cycle of Arctic aerosol number and size distributions, Atmos Chem Phys, 16, 3665-3682, 10.5194/acp-16-3665-2016, 2016.

Dastoor, A. P., Davignon, D., Theys, N., Van Roozendael, M., Steffen, A., and Ariya, P. A.: Modeling Dynamic Exchange of Gaseous Elemental Mercury at Polar Sunrise, Environmental Science & Technology, 42, 5183-5188, 10.1021/es800291w, 2008.

630   Dastoor, A. P., and Durnford, D. A.: Arctic Ocean: Is It a Sink or a Source of Atmospheric Mercury?, Environmental Science & Technology, 48, 1707-1717, 10.1021/es404473e, 2014.

Dibb, J. E., Arsenault, M., Peterson, M. C., and Honrath, R. E.: Fast nitrogen oxide photochemistry in Summit, Greenland snow, Atmospheric Environment, 36, 2501-2511, 10.1016/s1352-2310(02)00130-9, 2002.

DiMento, B. P., Mason, R. P., Brooks, S., and Moore, C.: The impact of sea ice on the air-sea exchange of mercury in the Arctic Ocean, Deep Sea Research Part I: Oceanographic Research Papers, 144, 28-38, https://doi.org/10.1016/j.dsr.2018.12.001, 2019.

640   Donohoue, D. L., Bauer, D., Cossairt, B., and Hynes, A. J.: Temperature and pressure dependent rate coefficients for the reaction of Hg with Br and the reaction of Br with Br: A pulsed laser photolysis-pulsed laser induced fluorescence study, Journal of Physical Chemistry A, 110, 6623-6632, 10.1021/jp054688j, 2006.

Douglas, T. A., and Blum, J. D.: Mercury Isotopes Reveal Atmospheric Gaseous Mercury Deposition Directly to the Arctic Coastal Snowpack, Environmental Science & Technology Letters, 6, 235-242, 10.1021/acs.estlett.9b00131, 2019.

Draxler, R. R., and Hess, G. D.: An overview of the HYSPLIT_4 modelling system for trajectories, dispersion and deposition, Australian Meteorological Magazine, 47, 295-308, 1998.

650   Drinovec, L., Močnik, G., Zotter, P., Prévôt, A. S. H., Ruckstuhl, C., Coz, E., Rupakheti, M., Sciare, J., Müller, T., Wiedensohler, A., and Hansen, A. D. A.: The "dual-spot" Aethalometer: an improved measurement of aerosol black carbon with real-time loading compensation, Atmos. Meas. Tech., 8, 1965-1979, 10.5194/amt-8-1965-2015, 2015.

Durnford, D., and Dastoor, A.: The behavior of mercury in the cryosphere: A review of what we know from observations, Journal of Geophysical Research, 116, 10.1029/2010jd014809, 2011.

Faïn, X., Obrist, D., Hallar, A. G., McCubbin, I., and Rahn, T.: High levels of reactive gaseous mercury observed at a high elevation research laboratory in the Rocky Mountains, Atmos. Chem. Phys., 9, 8049-8060, 10.5194/acp-9-8049-2009, 2009.

660   Freud, E., Krejci, R., Tunved, P., Leaitch, R., Nguyen, Q. T., Massling, A., Skov, H., and Barrie, L.: Pan-Arctic aerosol number size distributions: seasonality and transport patterns, Atmos Chem Phys, 17, 8101-8128, 10.5194/acp-17-8101-2017, 2017.

Frey, M. M., Norris, S. J., Brooks, I. M., Anderson, P. S., Nishimura, K., Yang, X., Jones, A. E., Nerentorp Mastromonaco, M. G., Jones, D. H., and Wolff, E. W.: First direct observation of sea salt aerosol production from blowing snow above sea ice, Atmos. Chem. Phys., 20, 2549-2578, 10.5194/acp-20-2549-2020, 2020.

Friedli, H. R., Arellano, A. F., Cinnirella, S., and Pirrone, N.: Initial Estimates of Mercury Emissions to the Atmosphere from Global Biomass Burning, Environmental Science & Technology, 43, 3507-3513, 10.1021/es802703g, 2009.

670   Fu, X., Maruszczak, N., Heimbürger, L. E., Sauvage, B., Gheusi, F., Prestbo, E. M., and Sonke, J. E.: Atmospheric mercury speciation dynamics at the high-altitude Pic du Midi Observatory, southern France, Atmos. Chem. Phys., 16, 5623-5639, 10.5194/acp-16-5623-2016, 2016.

Giordano, M. R., Kalnajs, L. E., Goetz, J. D., Avery, A. M., Katz, E., May, N. W., Leemon, A., Mattson, C., Pratt, K. A., and DeCarlo, P.
675   F.: The importance of blowing snow to halogen-containing aerosol in coastal Antarctica: influence of source region versus wind speed, Atmos. Chem. Phys., 18, 16689-16711, 10.5194/acp-18-16689-2018, 2018.

Goodsite, M. E., Plane, J. M. C., and Skov, H.: A theoretical study of the oxidation of Hg-0 to HgBr2 in the troposphere, Environmental Science & Technology, 38, 1772-1776, 10.1021/es034680s, 2004.
680

Goodsite, M. E., Plane, J. M. C., and Skov, H.: Correction to A Theoretical Study of the Oxidation of Hg0 to HgBr2 in the Troposphere, Environmental Science & Technology, 46, 5262-5262, 10.1021/es301201c, 2012.

Gratz, L. E., Ambrose, J. L., Jaffe, D. A., Shah, V., Jaegle, L., Stutz, J., Festa, J., Spolaor, M., Tsai, C., Selin, N. E., Song, S., Zhou, X.,
685   Weinheimer, A. J., Knapp, D. J., Montzka, D. D., Flocke, F. M., Campos, T. L., Apel, E., Hornbrook, R., Blake, N. J., Hall, S., Tyndall, G. S., Reeves, M., Stechman, D., and Stell, M.: Oxidation of mercury by bromine in the subtropical Pacific free troposphere, Geophysical Research Letters, 42, 10494-10502, 10.1002/2015gl066645, 2015.

Greene, C. A., Gwyther, D. E., and Blankenship, D. D.: Antarctic Mapping Tools for MATLAB, Computers & Geosciences, 104, 151-157,
690   10.1016/j.cageo.2016.08.003, 2017.

Arctic Sea Ice: https://www.mathworks.com/matlabcentral/fileexchange/56923-arctic-sea-ice), access: 2020-01-26, 2020.

Halfacre, J. W., Shepson, P. B., and Pratt, K. A.: pH-dependent production of molecular chlorine, bromine, and iodine from frozen saline
695   surfaces, Atmos. Chem. Phys., 19, 4917-4931, 10.5194/acp-19-4917-2019, 2019.

Hara, K., Osada, K., Yabuki, M., Takashima, H., Theys, N., and Yamanouchi, T.: Important contributions of sea-salt aerosols to atmospheric bromine cycle in the Antarctic coasts, Scientific Reports, 8, 13852, 10.1038/s41598-018-32287-4, 2018.

700   Helmig, D., Oltmans, S. J., Carlson, D., Lamarque, J.-F., Jones, A., Labuschagne, C., Anlauf, K., and Hayden, K.: A review of surface ozone in the polar regions, Atmospheric Environment, 41, 5138-5161, https://doi.org/10.1016/j.atmosenv.2006.09.053, 2007.

Hirdman, D., Aspmo, K., Burkhart, J. F., Eckhardt, S., Sodemann, H., and Stohl, A.: Transport of mercury in the Arctic atmosphere: Evidence for a spring-time net sink and summer-time source, Geophysical Research Letters, 36, 10.1029/2009gl038345, 2009.
705

Holmes, C. D., Jacob, D. J., and Yang, X.: Global lifetime of elemental mercury against oxidation by atomic bromine in the free troposphere, Geophysical Research Letters, 33, 10.1029/2006gl027176, 2006.

Holmes, C. D., Jacob, D. J., Corbitt, E. S., Mao, J., Yang, X., Talbot, R., and Slemr, F.: Global atmospheric model for mercury including
710   oxidation by bromine atoms, Atmos. Chem. Phys., 10, 12037-12057, 10.5194/acp-10-12037-2010, 2010.

Igel, A. L., Ekman, A. M. L., Leck, C., Tjernström, M., Savre, J., and Sedlar, J.: The free troposphere as a potential source of arctic boundary layer aerosol particles, Geophysical Research Letters, 44, 7053-7060, 10.1002/2017gl073808, 2017.

715   Jacob, D. J., Crawford, J. H., Maring, H., Clarke, A. D., Dibb, J. E., Emmons, L. K., Ferrare, R. A., Hostetler, C. A., Russell, P. B., Singh, H. B., Thompson, A. M., Shaw, G. E., McCauley, E., Pederson, J. R., and Fisher, J. A.: The Arctic Research of the Composition of the Troposphere from Aircraft and Satellites (ARCTAS) mission: design, execution, and first results, Atmos. Chem. Phys., 10, 5191-5212, 10.5194/acp-10-5191-2010, 2010.

720   Jiang, S., Ye, A., and Xiao, C.: The temperature increase in Greenland has accelerated in the past five years, Global and Planetary Change, 194, 103297, https://doi.org/10.1016/j.gloplacha.2020.103297, 2020.

Jiskra, M., Sonke, J. E., Agnan, Y., Helmig, D., and Obrist, D.: Insights from mercury stable isotopes on terrestrial–atmosphere exchange of Hg(0) in the Arctic tundra, Biogeosciences, 16, 4051-4064, 10.5194/bg-16-4051-2019, 2019.
725

Kaleschke, L., Richter, A., Burrows, J., Afe, O., Heygster, G., Notholt, J., Rankin, A. M., Roscoe, H. K., Hollwedel, J., Wagner, T., and Jacobi, H. W.: Frost flowers on sea ice as a source of sea salt and their influence on tropospheric halogen chemistry, Geophysical Research Letters, 31, 10.1029/2004gl020655, 2004.

730 Kamp, J., Skov, H., Jensen, B., and Sorensen, L. L.: Fluxes of gaseous elemental mercury (GEM) in the High Arctic during atmospheric mercury depletion events (AMDEs), Atmos Chem Phys, 18, 6923-6938, 10.5194/acp-18-6923-2018, 2018.

Landis, M. S., Stevens, R. K., Schaedlich, F., and Prestbo, E. M.: Development and characterization of an annular denuder methodology for the measurement of divalent inorganic reactive gaseous mercury in ambient air, Environmental Science & Technology, 36, 3000-735 3009, 10.1021/es015887t, 2002.

Laurier, F. J. G.: Reactive gaseous mercury formation in the North Pacific Ocean's marine boundary layer: A potential role of halogen chemistry, Journal of Geophysical Research, 108, 10.1029/2003jd003625, 2003.

740 Law, K. S., Stohl, A., Quinn, P. K., Brock, C. A., Burkhart, J. F., Paris, J.-D., Ancellet, G., Singh, H. B., Roiger, A., Schlager, H., Dibb, J., Jacob, D. J., Arnold, S. R., Pelon, J., and Thomas, J. L.: Arctic Air Pollution: New Insights from POLARCAT-IPY, Bulletin of the American Meteorological Society, 95, 1873-1895, 10.1175/bams-d-13-00017.1, 2014.

Lindberg, S. E., Brooks, S., Lin, C. J., Scott, K. J., Landis, M. S., Stevens, R. K., Goodsite, M., and Richter, A.: Dynamic oxidation of 745 gaseous mercury in the Arctic troposphere at polar sunrise, Environmental Science & Technology, 36, 1245-1256, 10.1021/es0111941, 2002.

Lu, J. Y., Schroeder, W. H., Barrie, L. A., Steffen, A., Welch, H. E., Martin, K., Lockhart, L., Hunt, R. V., Boila, G., and Richter, A.: Magnification of atmospheric mercury deposition to polar regions in springtime: The link to tropospheric ozone depletion 750 chemistry, Geophysical Research Letters, 28, 3219-3222, 10.1029/2000gl012603, 2001.

Macdonald, R. W., and Loseto, L. L.: Are Arctic Ocean ecosystems exceptionally vulnerable to global emissions of mercury? A call for emphasised research on methylation and the consequences of climate change, Environ. Chem., 7, 133-138, 10.1071/en09127, 2010.

755
Monks, P. S., Archibald, A. T., Colette, A., Cooper, O., Coyle, M., Derwent, R., Fowler, D., Granier, C., Law, K. S., Mills, G. E., Stevenson, D. S., Tarasova, O., Thouret, V., von Schneidemesser, E., Sommariva, R., Wild, O., and Williams, M. L.: Tropospheric ozone and its precursors from the urban to the global scale from air quality to short-lived climate forcer, Atmos Chem Phys, 15, 8889-8973, 10.5194/acp-15-8889-2015, 2015.

760
Muntean, M., Janssens-Maenhout, G., Song, S., Giang, A., Selin, N. E., Zhong, H., Zhao, Y., Olivier, J. G. J., Guizzardi, D., Crippa, M., Schaaf, E., and Dentener, F.: Evaluating EDGARv4.tox2 speciated mercury emissions ex-post scenarios and their impacts on modelled global and regional wet deposition patterns, Atmospheric Environment, 184, 56-68, https://doi.org/10.1016/j.atmosenv.2018.04.017, 2018.

765
Møller, A. K., Barkay, T., Al-Soud, W. A., Sørensen, S. J., Skov, H., and Kroer, N.: Diversity and characterization of mercury-resistant bacteria in snow, freshwater and sea-ice brine from the High Arctic, FEMS Microbiology Ecology, 75, 390-401, 10.1111/j.1574-6941.2010.01016.x, 2011.

770 Nguyen, Q. T., Glasius, M., Sorensen, L. L., Jensen, B., Skov, H., Birmili, W., Wiedensohler, A., Kristensson, A., Nojgaard, J. K., and Massling, A.: Seasonal variation of atmospheric particle number concentrations, new particle formation and atmospheric oxidation capacity at the high Arctic site Villum Research Station, Station Nord, Atmos Chem Phys, 16, 11319-11336, 10.5194/acp-16-11319-2016, 2016.

775 Obrist, D., Tas, E., Peleg, M., Matveev, V., Faïn, X., Asaf, D., and Luria, M.: Bromine-induced oxidation of mercury in the mid-latitude atmosphere, Nature Geoscience, 4, 22-26, 10.1038/ngeo1018, 2010.

Pal, B., and Ariya, P. A.: Studies of ozone initiated reactions of gaseous mercury: kinetics, product studies, and atmospheric implications, Physical Chemistry Chemical Physics, 6, 572-579, 10.1039/B311150D, 2004.

780

Atmospheric
Chemistry
and Physics
Discussions

Park, J.-D., and Zheng, W.: Human Exposure and Health Effects of Inorganic and Elemental Mercury, J Prev Med Public Health, 45, 344-352, 10.3961/jpmph.2012.45.6.344, 2012.

Peterson, P. K., Pöhler, D., Sihler, H., Zielcke, J., General, S., Frieß, U., Platt, U., Simpson, W. R., Nghiem, S. V., Shepson, P. B., Stirm, B. H., Dhaniyala, S., Wagner, T., Caulton, D. R., Fuentes, J. D., and Pratt, K. A.: Observations of bromine monoxide transport in the Arctic sustained on aerosol particles, Atmos. Chem. Phys., 17, 7567-7579, 10.5194/acp-17-7567-2017, 2017.

Peterson, P. K., Pöhler, D., Zielcke, J., General, S., Frieß, U., Platt, U., Simpson, W. R., Nghiem, S. V., Shepson, P. B., Stirm, B. H., and Pratt, K. A.: Springtime Bromine Activation over Coastal and Inland Arctic Snowpacks, ACS Earth and Space Chemistry, 2, 1075-1086, 10.1021/acsearthspacechem.8b00083, 2018.

Pfaffhuber, K. A., Berg, T., Hirdman, D., and Stohl, A.: Atmospheric mercury observations from Antarctica: seasonal variation and source and sink region calculations, Atmos Chem Phys, 12, 3241-3251, 10.5194/acp-12-3241-2012, 2012.

Pirrone, N., Cinnirella, S., Feng, X., Finkelman, R. B., Friedli, H. R., Leaner, J., Mason, R., Mukherjee, A. B., Stracher, G. B., Streets, D. G., and Telmer, K.: Global mercury emissions to the atmosphere from anthropogenic and natural sources, Atmos Chem Phys, 10, 5951-5964, 10.5194/acp-10-5951-2010, 2010.

Quack, B., and Wallace, D. W. R.: Air-sea flux of bromoform: Controls, rates, and implications, Global Biogeochemical Cycles, 17, 10.1029/2002gb001890, 2003.

Rolph, G., Stein, A., and Stunder, B.: Real-time Environmental Applications and Display sYstem: READY, Environmental Modelling & Software, 95, 210-228, 10.1016/j.envsoft.2017.06.025, 2017.

Sander, R.: Compilation of Henry's law constants (version 4.0) for water as solvent, Atmos. Chem. Phys., 15, 4399-4981, 10.5194/acp-15-4399-2015, 2015.

Schacht, J., Heinold, B., Quaas, J., Backman, J., Cherian, R., Ehrlich, A., Herber, A., Huang, W. T. K., Kondo, Y., Massling, A., Sinha, P. R., Weinzierl, B., Zanatta, M., and Tegen, I.: The importance of the representation of air pollution emissions for the modeled distribution and radiative effects of black carbon in the Arctic, Atmos. Chem. Phys., 19, 11159-11183, 10.5194/acp-19-11159-2019, 2019.

Schmeisser, L., Backman, J., Ogren, J. A., Andrews, E., Asmi, E., Starkweather, S., Uttal, T., Fiebig, M., Sharma, S., Eleftheriadis, K., Vratolis, S., Bergin, M., Tunved, P., and Jefferson, A.: Seasonality of aerosol optical properties in the Arctic, Atmos. Chem. Phys., 18, 11599-11622, 10.5194/acp-18-11599-2018, 2018.

Schroeder, W. H., Anlauf, K. G., Barrie, L. A., Lu, J. Y., Steffen, A., Schneeberger, D. R., and Berg, T.: Arctic springtime depletion of mercury, Nature, 394, 331-332, 10.1038/28530, 1998.

Schulz, H., Zanatta, M., Bozem, H., Leaitch, W. R., Herber, A. B., Burkart, J., Willis, M. D., Kunkel, D., Hoor, P. M., Abbatt, J. P. D., and Gerdes, R.: High Arctic aircraft measurements characterising black carbon vertical variability in spring and summer, Atmos. Chem. Phys., 19, 2361-2384, 10.5194/acp-19-2361-2019, 2019.

Semane, N., Peuch, V. H., El Amraoui, L., Bencherif, H., Massart, S., Cariolle, D., Attie, J. L., and Abida, R.: An observed and analysed stratospheric ozone intrusion over the high Canadian Arctic UTLS region during the summer of 2003, Quarterly Journal of the Royal Meteorological Society, 133, 171-178, 10.1002/qj.141, 2007.

Shah, V., and Jaeglé, L.: Subtropical subsidence and surface deposition of oxidized mercury produced in the free troposphere, Atmos. Chem. Phys., 17, 8999-9017, 10.5194/acp-17-8999-2017, 2017.

Simpson, W. R., Brown, S. S., Saiz-Lopez, A., Thornton, J. A., and Glasow, R.: Tropospheric halogen chemistry: sources, cycling, and impacts, Chem Rev, 115, 4035-4062, 10.1021/cr5006638, 2015.

Skov, H., Christensen, J. H., Goodsite, M. E., Heidam, N. Z., Jensen, B., Wahlin, P., and Geernaert, G.: Fate of elemental mercury in the arctic during atmospheric mercury depletion episodes and the load of atmospheric mercury to the arctic, Environmental Science & Technology, 38, 2373-2382, 10.1021/es030080h, 2004.

Atmospheric
Chemistry
and Physics

Discussions

Skov, H., Brooks, S., Goodsite, M., Lindberg, S., Meyers, T., Landis, M., Larsen, M., Jensen, B., McConville, G., and Christensen, J.: Fluxes of reactive gaseous mercury measured with a newly developed method using relaxed eddy accumulation, Atmospheric Environment, 40, 5452-5463, 10.1016/j.atmosenv.2006.04.061, 2006.

Skov, H., Hjorth, J., Nordstrøm, C., Jensen, B., Christoffersen, C., Bech Poulsen, M., Baldtzer Liisberg, J., Beddows, D., Dall'Osto, M., and Christensen, J.: The variability in Gaseous Elemental Mercury at Villum Research Station, Station Nord in North Greenland from 1999 to 2017, Atmos. Chem. Phys. Discuss., 2020, 1-22, 10.5194/acp-2019-912, 2020.

Soerensen, A. L., Skov, H., Jacob, D. J., Soerensen, B. T., and Johnson, M. S.: Global Concentrations of Gaseous Elemental Mercury and Reactive Gaseous Mercury in the Marine Boundary Layer, Environmental Science & Technology, 44, 7425-7430, 10.1021/es903839n, 2010.

Sommar, J., Andersson, M. E., and Jacobi, H. W.: Circumpolar measurements of speciated mercury, ozone and carbon monoxide in the boundary layer of the Arctic Ocean, Atmos Chem Phys, 10, 5031-5045, 10.5194/acp-10-5031-2010, 2010.

Steen, A. O., Berg, T., Dastoor, A. P., Durnford, D. A., Engelsen, O., Hole, L. R., and Pfaffhuber, K. A.: Natural and anthropogenic atmospheric mercury in the European Arctic: a fractionation study, Atmos Chem Phys, 11, 6273-6284, 10.5194/acp-11-6273-2011, 2011.

Steffen, A., Bottenheim, J., Cole, A., Ebinghaus, R., Lawson, G., and Leaitch, W. R.: Atmospheric mercury speciation and mercury in snow over time at Alert, Canada, Atmos Chem Phys, 14, 2219-2231, 10.5194/acp-14-2219-2014, 2014.

Steffen, A., Lehnherr, I., Cole, A., Ariya, P., Dastoor, A., Durnford, D., Kirk, J., and Pilote, M.: Atmospheric mercury in the Canadian Arctic. Part I: a review of recent field measurements, Sci Total Environ, 509-510, 3-15, 10.1016/j.scitotenv.2014.10.109, 2015.

Stephens, C. R., Shepson, P. B., Steffen, A., Bottenheim, J. W., Liao, J., Huey, L. G., Apel, E., Weinheimer, A., Hall, S. R., Cantrell, C., Sive, B. C., Knapp, D. J., Montzka, D. D., and Hornbrook, R. S.: The relative importance of chlorine and bromine radicals in the oxidation of atmospheric mercury at Barrow, Alaska, Journal of Geophysical Research: Atmospheres, 117, n/a-n/a, 10.1029/2011jd016649, 2012.

Stern, G. A., Macdonald, R. W., Outridge, P. M., Wilson, S., Chetelat, J., Cole, A., Hintelmann, H., Loseto, L. L., Steffen, A., Wang, F., and Zdanowicz, C.: How does climate change influence Arctic mercury?, Sci Total Environ, 414, 22-42, 10.1016/j.scitotenv.2011.10.039, 2012.

Stohl, A.: Computation, accuracy and applications of trajectories - A review and bibliography, Atmospheric Environment, 32, 947-966, 10.1016/s1352-2310(97)00457-3, 1998.

Stroeve, J. C., Serreze, M. C., Holland, M. M., Kay, J. E., Malanik, J., and Barrett, A. P.: The Arctic's rapidly shrinking sea ice cover: a research synthesis, Climatic Change, 110, 1005-1027, 10.1007/s10584-011-0101-1, 2012.

Sturges, W. T., Cota, G. F., and Buckley, P. T.: Bromoform emission from Arctic ice algae, Nature, 358, 660-662, 10.1038/358660a0, 1992.

Swartzendruber, P. C., Jaffe, D. A., Prestbo, E. M., Weiss-Penzias, P., Selin, N. E., Park, R., Jacob, D. J., Strode, S., and Jaeglé, L.: Observations of reactive gaseous mercury in the free troposphere at the Mount Bachelor Observatory, Journal of Geophysical Research, 111, 10.1029/2006jd007415, 2006.

Talbot, R., Mao, H., Scheuer, E., Dibb, J., and Avery, M.: Total depletion of Hg degrees in the upper troposphere-lower stratosphere, Geophysical Research Letters, 34, 5, 10.1029/2007gl031366, 2007.

Tunved, P., Ström, J., and Krejci, R.: Arctic aerosol life cycle: linking aerosol size distributions observed between 2000 and 2010 with air mass transport and precipitation at Zeppelin station, Ny-Ålesund, Svalbard, Atmos Chem Phys, 13, 3643-3660, 10.5194/acp-13-3643-2013, 2013.

UNEP: Minamata Convention on Mercury: http://www.mercuryconvention.org/Convention/tabid/3426/Default.aspx access: 2020-11-12, 2013.

895   Walker, T. W., Jones, D. B. A., Parrington, M., Henze, D. K., Murray, L. T., Bottenheim, J. W., Anlauf, K., Worden, J. R., Bowman, K. W., Shim, C., Singh, K., Kopacz, M., Tarasick, D. W., Davies, J., von der Gathen, P., Thompson, A. M., and Carouge, C. C.: Impacts of midlatitude precursor emissions and local photochemistry on ozone abundances in the Arctic, Journal of Geophysical Research-Atmospheres, 117, 10.1029/2011jd016370, 2012.

900   Wang, S., McNamara, S. M., Moore, C. W., Obrist, D., Steffen, A., Shepson, P. B., Staebler, R. M., Raso, A. R. W., and Pratt, K. A.: Direct detection of atmospheric atomic bromine leading to mercury and ozone depletion, Proc Natl Acad Sci U S A, 116, 14479-14484, 10.1073/pnas.1900613116, 2019.

        Weingartner, E., Saathoff, H., Schnaiter, M., Streit, N., Bitnar, B., and Baltensperger, U.: Absorption of light by soot particles: determination of the absorption coefficient by means of aethalometers, Journal of Aerosol Science, 34, 1445-1463,
905   https://doi.org/10.1016/S0021-8502(03)00359-8, 2003.

        Winiger, P., Barrett, T. E., Sheesley, R. J., Huang, L., Sharma, S., Barrie, L. A., Yttri, K. E., Evangeliou, N., Eckhardt, S., Stohl, A., Klimont, Z., Heyes, C., Semiletov, I. P., Dudarev, O. V., Charkin, A., Shakhova, N., Holmstrand, H., Andersson, A., and Gustafsson, Ö.: Source apportionment of circum-Arctic atmospheric black carbon from isotopes and modeling, Science Advances, 5, eaau8052,
910   10.1126/sciadv.aau8052, 2019.

        Yang, X., Cox, R. A., Warwick, N. J., Pyle, J. A., Carver, G. D., O'Connor, F. M., and Savage, N. H.: Tropospheric bromine chemistry and its impacts on ozone: A model study, Journal of Geophysical Research: Atmospheres, 110, 10.1029/2005jd006244, 2005.

915   Zanatta, M., Laj, P., Gysel, M., Baltensperger, U., Vratolis, S., Eleftheriadis, K., Kondo, Y., Dubuisson, P., Winiarek, V., Kazadzis, S., Tunved, P., and Jacobi, H. W.: Effects of mixing state on optical and radiative properties of black carbon in the European Arctic, Atmos. Chem. Phys., 18, 14037-14057, 10.5194/acp-18-14037-2018, 2018.